# Supporting Information

MCNTs@$MnO_2$ Nanocomposite Cathode Integrated with Soluble $O_2$-Carrier Co-salen in Electrolyte for High-Performance Li-Air Batteries

Xiaofei Hu,[†] Jianbin Wang,[†] Zifan Li,[†] Jiaqi Wang,[†] Duncan H. Gregory,[§] and Jun Chen*,[†]

[†]Key Laboratory of Advanced Energy Materials Chemistry (Ministry of Education) and State Key Laboratory of Elemento-Organic Chemistry, Collaborative Innovation Center of Chemical Science and Engineering, College of Chemistry, Nankai University, Tianjin 300071, China

[§]School of Chemistry, University of Glasgow, University Avenue, Glasgow G12 8QQ, UK.

Corresponding Author
*E-mail: chenabc@nankai.edu.cn

**Contents:**

## Preparation of the electrolyte

Tetraethylene glycol dimethyl ether (TEGDME) was purchased from Sigma-Aldrich and dried over 4 Å molecular sieves. Lithium bis(trifluoromethanesulfonyl)imide (LiTFSI) was used as received from J&K Chemical. $Co^{II}$-salen was from Sigma-Aldrich. The electrolyte was prepared by mixing the solvent, LiTFSI, and $Co^{II}$-salen in the Ar-filled glovebox (Mikrouna Universal 2440/750). The concentration of LiTFSI in TEGDME was 1 mol $L^{-1}$. The $Co^{II}$-salen in TEGDME was controlled from 1 to 5 and 20 mmol $L^{-1}$.

**Synthesis of MCNTs@$MnO_2$**

The composite of multi-wall CNT@$MnO_2$ (MCNTs@$MnO_2$) was synthesized via two-step sonication. For step 1, commercial multi-wall CNTs (5.5 mg, Beijing Cnano Technology Limited) were added to the aqueous solution of 1.84 M $H_2SO_4$ (11 ml) and sonicated for 60 min at room temperature (~20 °C) in a plastic tube. For step 2, after we suction out acid liquor of 8 ml from the tube and add aqueous solution of 0.1 M $KMnO_4$ (8 ml) back, the original tube was sonicated for 60 min at room temperature (~20 °C). The preparation process is easily scaled by increasing the number of plastic tube. Once done, the contents was centrifuged with and DI water (deionized water) and absolute ethyl alcohol several times. Finally, the obtained products was dried at 100 °C overnight in ambient air. MCNTs@$MnO_2$-L was synthesized sonication for 180 min in step 2, and the other conditions are the same as MCNTs@$MnO_2$.

## Materials characterization

The composites of MCNT, MCNTs@$MnO_2$, MCNTs@$MnO_2$-L, and discharge product in Li–air batteries were characterized by powder X-ray diffraction (Rigaku MiniFlex600, Cu Kα radiation). The content of C in MWCNT@$MnO_2$ was calculated by Thermogravimetric analysis (TGA) with a heating rate 5 °C $min^{-1}$ from 20 °C to 760 °C in air atmosphere. The Brunauer-Emmett-Teller (BET) specific surface area was obtained by the $N_2$ adsorption–desorption isotherm at 77 K (BELSORP-mini instrument). Raman spectra of $Co^{II}$-salen with and without exposure to $O_2$ were collected on DXR, Thermo Fisher Scientific with excitation at 532 nm from an Ar-ion laser. The discharge products of LABs were characterized by powder X-ray diffraction (Rigaku MiniFlex600, Cu Kα radiation). The morphologies of the products were observed by field-emission scanning electron microscopy (SEM, JEOL JSM7500F) and transmission electron microscopy (TEM, Tecnai G2 F20).

## Electrochemical tests

The Electrochemical performance of nonaqueous Li–air was tested at room temperature using CR2032 coin-type batteries. These batteries consist of a lithium foil anode, a glass fiber separator (16 mm in diameter, 0.3 mm in thickness, porosity 92%–98%), and an air electrode. The cathode is one piece of Ni foam evenly coated by 90 wt% catalyst (MCNTs, MCNTs@$MnO_2$, or MCNTs@$MnO_2$-L) and 10 wt% polyvinylidene fluoride (PVdF). The electrolyte is 100 μl of 1 M LiTFSI (lithium bis-(trifluoromethanesulfonyl)-imide) in TEGDME (tetraethylene glycol dimethyl ether) with or without $Co^{II}$-salen. For cathodes, the total mass loading on the Ni foam

is 0.3 and 1.0 mg $cm^{-2}$ (the mass of each piece of Ni foam is about 22.6 mg). The battery capacity in this study is based on the mass of MCNTs or MCNTs@$MnO_2$ nanocomposite on cathode. Towards the same dischrge capacity, e.g. 0.3 mAh $cm^{-2}$, the mass of $Li_2O_2$ on cathodes is 0.26 mg $cm^{-2}$. All the batteries were assembled in a glove box (Mikrouna Universal 2440/750) with $H_2O$ and oxygen content < 2 ppm. The gas for battery operation is high-pure oxygen or dry air that is composed of 21 % of $O_2$ and 78% of $N_2$. After resting for 10 to 20 h, the batteries were subjected to galvanostatic discharge/charge on a LAND battery testing system at room temperature.

## Assembly of pouch-type LABs

Pouch-type LABs are assembled and investigated. They are made up of two porous fixture boards (8.0 × 12.0 $cm^2$), a plastic bag (8.0 × 13.0 $cm^2$, 0.30 g), a Li foil anode (7.5 × 10 $cm^2$, 0.28 g), a glass fiber separator (7.8 × 11.1 $cm^2$) containing electrolyte of 1 M LiTFSI/TEGDME and 5 mM Co-salen (2.00 g), and a carbon paper cathode (7.6 × 10.9 $cm^2$, 0.30 g) with 40 mg MCNTs@$MnO_2$. The total mass of pouch-type LABs is ~4.0 g except for the mass of electric wires and fixture boards. It is worth noting that one side of each plastic bag is punched with many pores for air transfer.

## Rotating-Disk-Electrode (RDE) measurements

The electrochemical characterization was conducted in a three-electrode electrochemical cell. The cell consists of a Pt foil (counter electrode), an Ag wire quasireference electrode (~3.1 V vs $Li^+$/Li), and a glass carbon (GC) electrode (a working electrode) loaded with samples. This GC is fixed in a rotating disk electrode

(RDE, GC disk with radius of 2.80 mm). The electrolyte is 1 M LiTFSI in TEGDME with different concentrations of $Co^{II}$-salen. The electrolyte was saturated with high-purity $O_2$ or Ar (Air Product, purity 99.995%). ORR test in $O_2$ was conducted using $O_2$ saturated electrolyte and purging the liquid level with Ar to guarantee that the consumed $O_2$ for $Li_2O_2$ formation comes from the electrolyte. For the preparation of catalyst films, the MCNTs or MCNTs@$MnO_2$ (10 mg) was ultrasonically dispersed into 1000 μL of 950:50 v/v isopropyl alcohol/neutralized nafion solution (5 wt%, Sigma-Aldrich) to form a black ink. Then, 7.0 μL of the ink (containing 70 μg of carbon) was loaded onto the GC electrode and naturally dried for 10 h. The carbon loading was ~0.284 mg $cm^{-2}$. In linear sweep voltammetry (LSV) test, the disk electrode was scanned at a scanning rate of 2 mV $s^{-1}$ with a rotating speed of 900 r $min^{-1}$.

## Powder electrochemical impedance spectroscopy (PEIS) measurements

We create a simple method of PEIS to value intrinsic electron transport kinetics of sample powders. The PEIS device consists of an anode case (20 mm in diameter and 0.25 mm in thickness) and a stainless steel spacer (1.0 mm in thickness) of 2032-coin type. Powder samples (with fixed mass of 6 mg) were pressed (10 kPa $cm^{-2}$) in the interlayer of the anode case and the stainless steel spacer. The following step is the same as electrochemical impedance spectroscopy (EIS) test that was measured on an AC voltage of 5 mV amplitude in the frequency range from 100 kHz to 100 mHz. The nanocomposite showed a much smaller semicircle (1.26 kΩ) than MCNTs/$MnO_2$

mixture (3.70 kΩ). This result suggests that MCNTs@$MnO_2$ has a higher electron transport through the interface of MCNTs and $MnO_2$ than that of MCNTs/$MnO_2$ mixture. Notably, MCNTs@$MnO_2$ nanocomposite and MCNTs/$MnO_2$ mixture has same $MnO_2$ content (57%), which is confirmed later.

## Apparent $O_2$ solubility caculation

According to the reaction of $2Li^+ + O_2 + 2e^- \leftrightarrow Li_2O_2$ and the formula of $C_{th}$ = 26800×n/M, capacity of 1675.1 mAh is output by comsuming 1 g of $O_2$. In the above formula, n is transfer electron number, 2; M is molecular weight, 32 g $mol^{-1}$. The discharge capacity with and without 5 mM Co-salen at 10 mA $g^{-1}$ is 0.0247 mAh and 0.0026 mAh, respectively, corresponding to $4.61\times10^{-7}$ mol and $4.85\times10^{-8}$ mol of $O_2$. In consideration of the electrolyte volume of 100 μL, we obtain the apparent $O_2$ solubility of 4.61 mM and 0.49 mM for 5 and 0 mM salen, respectively. In fact, the dissolved $O_2$ in the electrolyte could not be completely consumed, because of the existance of $O_2$ concentration gradient. Thus, the real value of $O_2$ solubility is higher than above apparent value.

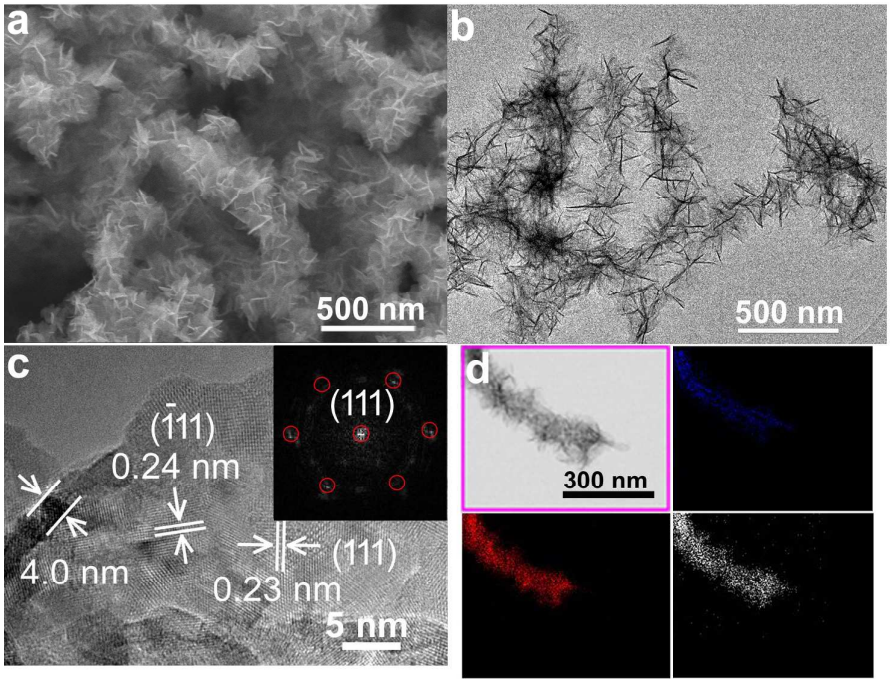


**Figure S1.** The morphology and crystal lattice of MCNTs@$MnO_2$-L. (a) SEM image, (b) TEM image, and (c) HRTEM images of MCNTs@$MnO_2$-L. (d) Energy-dispersive X-ray (EDX) mapping (of the C, Mn, and O elements) of MCNTs@$MnO_2$-L.

In comparison with coating time of 1.5 h, as the coating time went longer (3 h), we obtained the over coated composite (labeled as MCNTs@$MnO_2$-L), in which $MnO_2$ nanosheets wrapped outside and its diameter increased to ~230 nm. The EDX mappings of particular regions clearly show the core-shell structure of MCNTs@$MnO_2$-L consisting of inner MCNTs and outer $MnO_2$ layers.

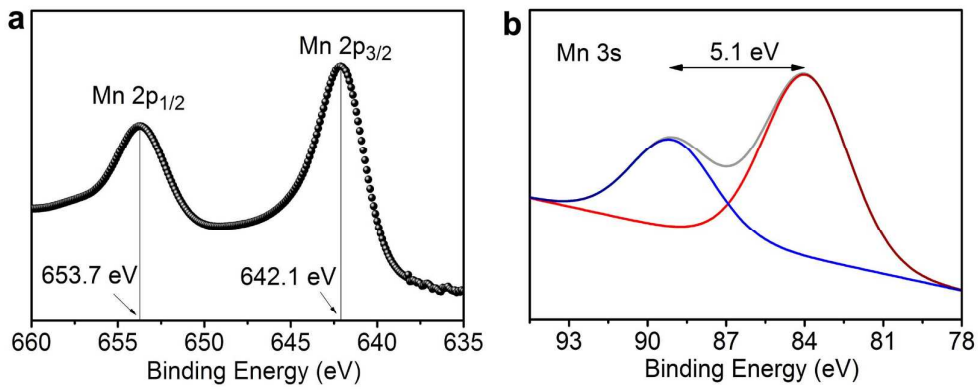


**Figure S2.** XPS survey of MCNTs@$MnO_2$: (a) Mn 2p, (b) Mn 3s.

We also applied surface elemental analysis by X-ray photoelectron spectroscopy (XPS) on MCNTs@$MnO_2$. The high-resolution Mn 2p core level spectra show that Mn $2p_{3/2}$ (642.1 eV) and Mn $2p_{1/2}$ (653.7 eV) show a spin energy separation of 11.6 eV, which is in agreement with the reported data for $MnO_2$.[1−4] The splitting width of the Mn 3s doublet peaks is 5.1 eV, indicating that its oxidation state is between 3.5−4.[5] This result is also consistent with soft X-ray spectroscope. The fact that Mn valence between 3.5−4 rather than 4 is probably caused by oxygen defects, which is good for ORR/OER catalysis.[6]

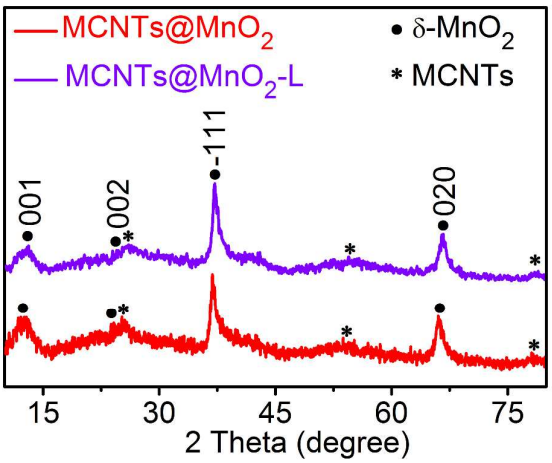


**Figure S3.** XRD of MCNTs@$MnO_2$ and MCNTs@$MnO_2$-L.

Soft X-ray absorption spectroscopies (SXAS) are used to reveal the valence bond transition during synthesis procedure of MCNTs@$MnO_2$ nanocomposite. At the carbon K-edge, we can obviously observe a significant increase in the peak absorption intensity around 289 eV as compared to MCNTs control, which is attributed to the C−O functional groups on MCNTs.[7] This suggested possible formation of C−O−Mn bonds in the composite materials. As the reaction time turns longer (MCNTs + $KMnO_4 \rightarrow CO_2\uparrow$ + MCNTs@$MnO_x$ + $K_2CO_3$), the peak intensity of C=C bond (~286 eV) decreases, because abundant C=C open along with more and more C-O-Mn (~289 eV) formation.[8,9] Besides, a lower adsorption intensity of the π* peak of ~286 eV (C−K edge) of the composites as compared to the MCNTs control is observed, suggesting possible electron transfer from Mn to MCNTs in the composite material.[10] The bond formations and charge transfer indicate the intimate couplings between $MnO_x$ coating layer and MCNTs. Based on the earlier reports of the O K-edge absorption spectra,[11,12] the first intense pre-edge peaks (530.4 eV and 533.0 eV) corresponds to the transition of O 1s electron to the hybridized state of Mn 3d and O 2p orbitals, whereas the broad higher energy peaks (around 545 eV) correspond to the transitions to hybridized states of O2p and Mn 4sp orbitals. Namely, peaks at 530.4 eV and 533.0 eV are from the electron jump of O1s to eg↑t2g↓ and eg↓of Mn3d orbits in MnOx. For the Mn ions in MCNTs@$MnO_2$ and MCNTs@$MnO_2$-L, the peaks at 640 to 645 eV and 654.5 eV are due to the respective electronic transitions from Mn $2p_{3/2}$ and $2p_{1/2}$ core level.[13] The peak intensity of Mn (IV, 642.0 eV and 644.4 eV) increases with reaction going, suggesting that the trace of Mn (II, 641.3 eV) and tiny of Mn (III, 643.0 eV) continuously transform to Mn (IV). According to the change of peak intensity in MCNTs@$MnO_2$ and MCNTs@$MnO_2$-L, proportion of Mn (IV) increase and proportion of Mn-ion with low valence state decreases, also indicating the transformation from Mn (II) and Mn (III) to Mn (IV). The data shown by SXAS suggest that a small amount of low-valence Mn-ion and large amount of Mn (IV) form at early stage of the synthesis reaction, and as reaction time prolongs, more and more C-O-Mn forms and the surviving low-valence Mn-ion continuously transform to Mn (IV).

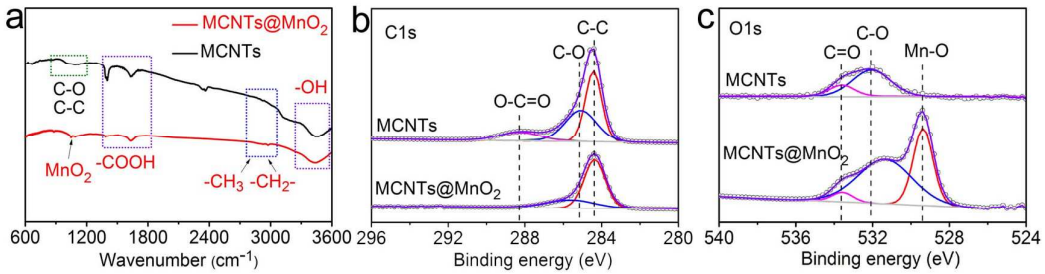


**Figure S4.** FT-IR and XPS of MCNTs and MCNTs@$MnO_2$ nanocomposite. (**a**) FT-IR of MCNTs and MCNTs@$MnO_2$. (b,c) XPS of (b) C1s and (c) O1s..

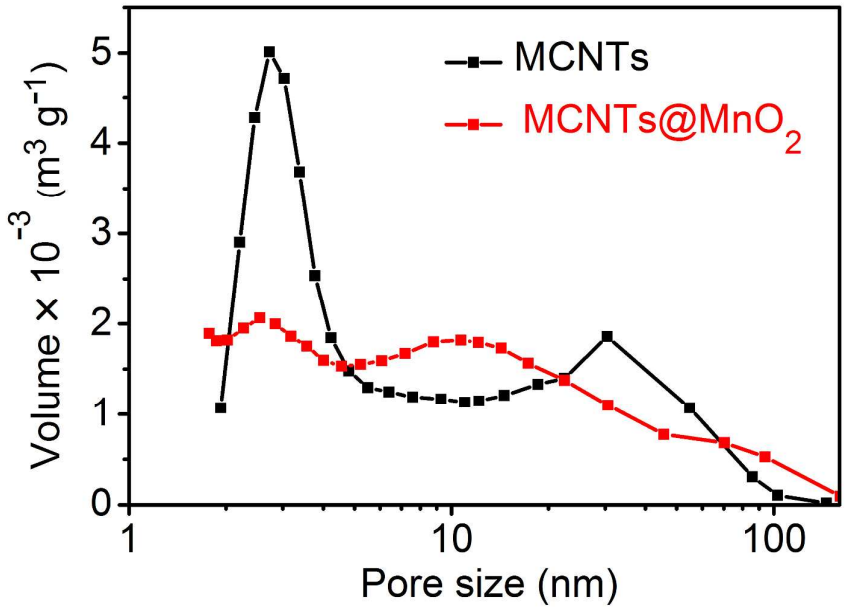


**Figure S5.** Pore distribution of MCNTs and MCNTs@$MnO_2$.

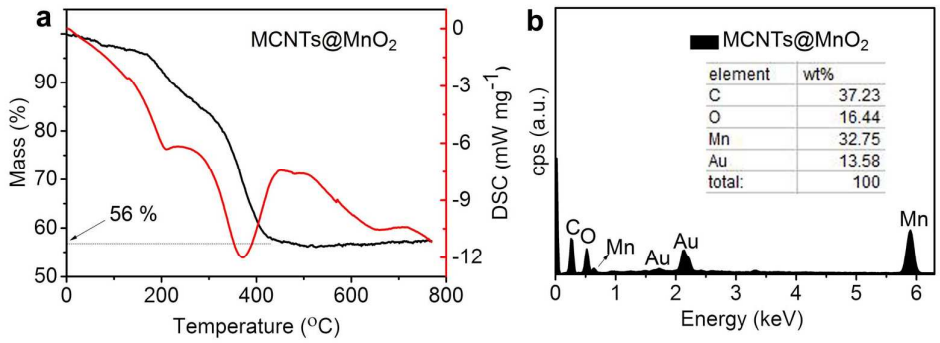


**Figure S6.** Thermal gravity analysis (TGA) curves and EDS spectra of MCNTs@$MnO_2$. (a) TGA curves below 780 °C measured with a heating rate of 5 °C $min^{-1}$ in air atmosphere. (b) EDS spectra. The content of C within the composite is ~43%.

Thermo-gravimetric analysis (TGA) of MWCNT@$MnO_2$ is shown above. Only ~4 wt% weight loss were observed until 173 °C, which result from the escape of adsorbed water and air. The fast weight losses until 450 °C mainly arise from the oxidation of MCNTs ($C + O_2 \rightarrow CO_2$), suggesting the mass content of carbon in the composite is about 43.0 wt%, which is in the agreement with large-scale EDX of the composite MCNTs@$MnO_2$.

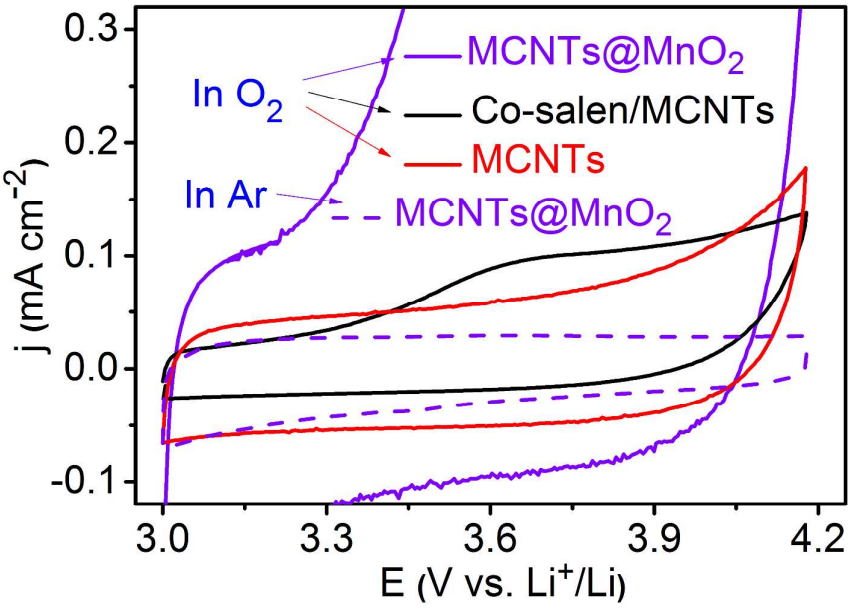


**Figure S7.** CV curves with speed of 1 mV $s^{-1}$. This figure combines amplifying curves in Figure 1h and CV curves of Co-salen/MCNTs. Co-salen/MCNTs stands for the LABs with 5 mM Co-salen in electrolyte and MCNT cathode.

Because the same amount of $Li_2O_2$ was deposited during discharge, the integrated area under the oxidation peaks for each electrode is identical in theory. In fact, the electrodes with Co-salen/MCNTs or MCNTs have poor catalytic activity towards $Li_2O_2$ decomposition and thus need higher voltage (>4.2 V) to oxidize $Li_2O_2$. So, the integrated areas under the oxidation peaks for each electrode between 3.0 and 4.2 V are not same. In order to eliminate the risk of electrolyte decomposition, the voltage window is limited below 4.2 V.

In addition, the weaker oxidation current and much higher onset potential of Co-salen/MCNTs than that of MCNTs@$MnO_2$, indicating poor catalytic activity of Co-salen/MCNTs towards $Li_2O_2$ decomposition.

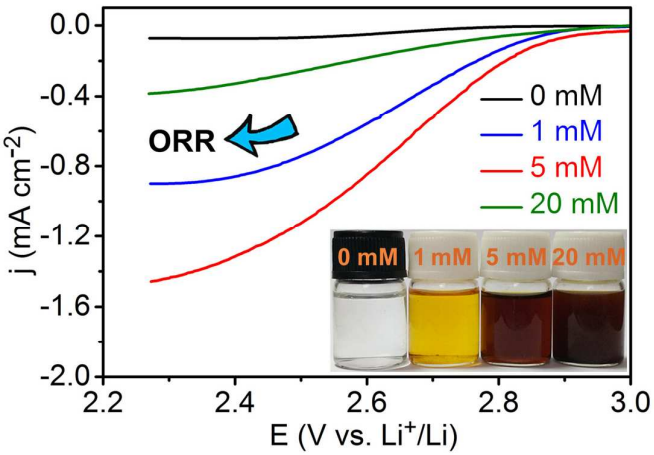


**Figure S8.** LSV curves under $O_2$ in electrolytes with different concentrations of $Co^{II}$-salen on MCNTs coated glassy carbon electrode at 900 r $min^{-1}$ and 2 mV $s^{-1}$. The inset is the photographs of 1 M LiTFSI/TEGDME electrolytes with different concentrations of $Co^{II}$-salen from 0 mM to 1, 5, and 20 mM.

The concentration of $Co^{II}$-salen in 1 M LiTFSI/TEGDME electrolyte is adjusted from 0 mM to 1, 5, and 20 mM and the colors gradually vary from light-colored to dark in the inset graph. The linear sweep voltammetry (LSV) of these electrolytes on MCNTs coated glassy carbon electrode is shown above. In comparison with other three concentrations, the electrolyte with 5 mM $Co^{II}$-salen exhibits more positive ORR onset potential as well as higher catalytic current density. Therefore, the optimal concentration of $Co^{II}$-salen in the TEGDME based electrolyte is 5 mM.

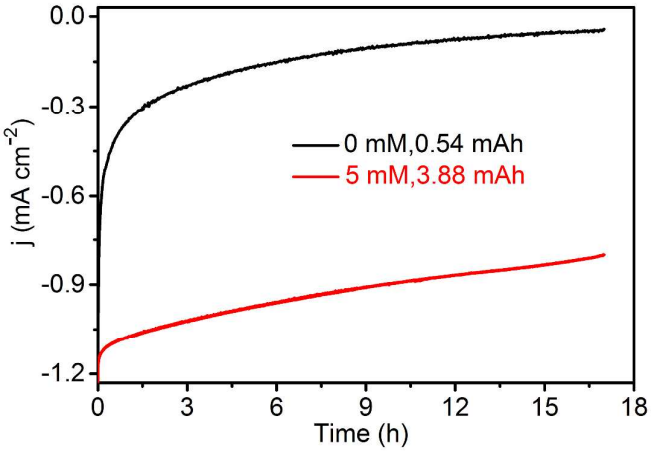


**Figure S9.** Current-time curves on MCNTs coated glassy carbon electrode at 400 r $min^{-1}$. The supporting electrolyte is 20 mL of 0 mM or 5 mM $Co^{II}$-salen/TEGDME electrolytes. The fixed potential is 2.5 V vs. $Li^+$/Li. It should be mentioned that electrolyte surface is purged by Ar after the electrolyte has been saturated by $O_2$. The integrated areas between current density and time are 3.88 mAh (5 mM Co-salen) and 0.54 mAh (0 mM Co-salen).

In order to invoid the limitation by pore volume and surface passivation of active sites of cathode, we add an experiment on the glass carbon electrode to study the effect of the Co-salen $O_2$-carrier on ORR in electrolytes of 0 mM or 5 mM $Co^{II}$-salen/TEGDME. By fixing the reduction potential of 2.5 V vs. $Li^+$/Li for 17 h, the oxygen reduction current of $O_2$-saturated electrolyte with Co-salen (0.80 mA $cm^{-2}$) is much larger than that without Co-salen (0.04 mA $cm^{-2}$). The capacities with and without Co-salen are 3.88 mAh and 0.54 mAh, respectively. At the potential of 2.5 V vs. $Li^+$/Li, $O_2$ and $(Co\text{-}salen)_2$-$O_2$ rather than Co-salen self could be reduced. So, above capacity only relates to $O_2$ consumption. Correspondingly, the apparent $O_2$-solubility without Co-salen is 0.51 mM, which is much smaller than that with Co-salen. Those data imply the much improved catalytic activity of $Co^{II}$-salen and its high reversible $O_2$ uptake capability. Notably, the value of apparent $O_2$-solubility without Co-salen is close to that calculated by battery discharge (0.49 mM) in Figure 2e.

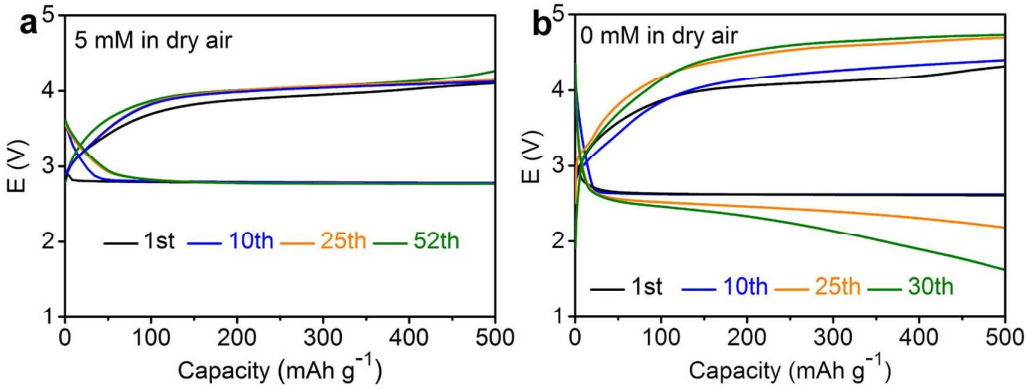


**Figure S10.** Discharge/charge profiles of LABs (a) with (b) without $Co^{II}$-salen in electrolytes in dry air. Rate, 250 mA $g^{-1}$ (0.075 mA $cm^{-2}$). The capacity of 500 mAh $g^{-1}$ corresponds to 0.15 mAh $cm^{-2}$.

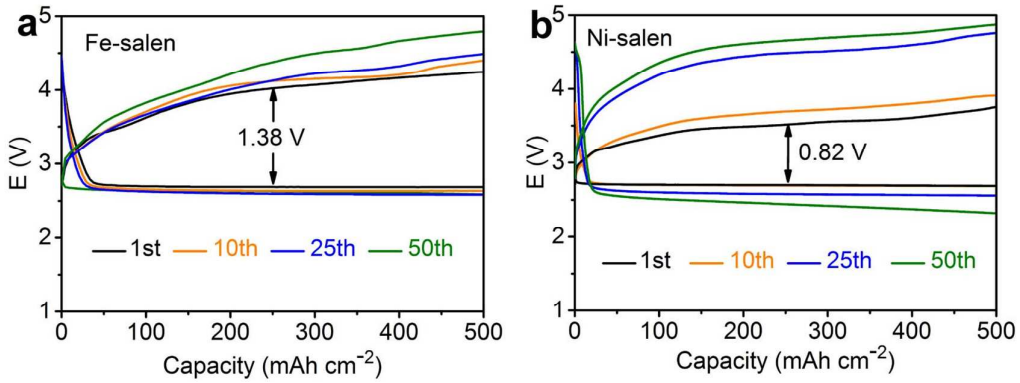


**Figure S11.** Electrochemical performance of LABs with (a) 5 mM $Fe^{II}$-salen and (b) 5 mM $Ni^{II}$-salen in electrolytes at 250 mA $g^{-1}$ (0.075 mA $cm^{-2}$).

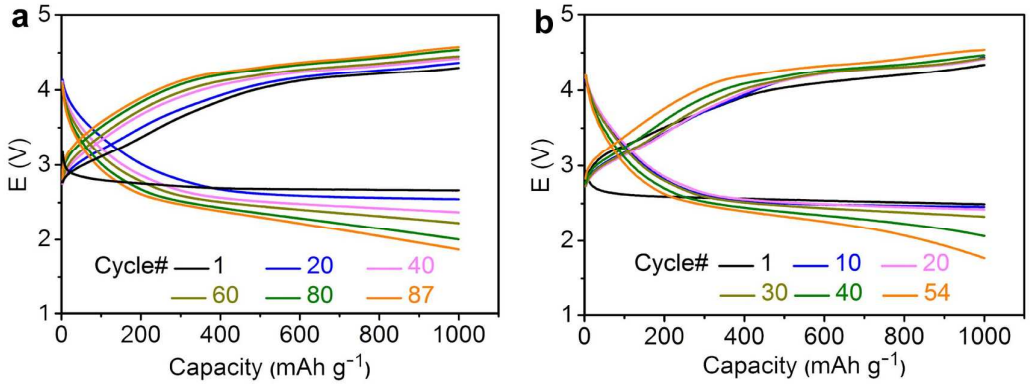


**Figure S12.** Charge/discharge cures of LABs with Co-salen/MCNTs@$MnO_2$ at different current densities with fixed capacity of 1000 mAh $g^{-1}$ (0.30 mAh $cm^{-2}$): (a) 1 A $g^{-1}$ (0.30 mA $cm^{-2}$), (b) 2 A $g^{-1}$ (0.60 mA $cm^{-2}$).

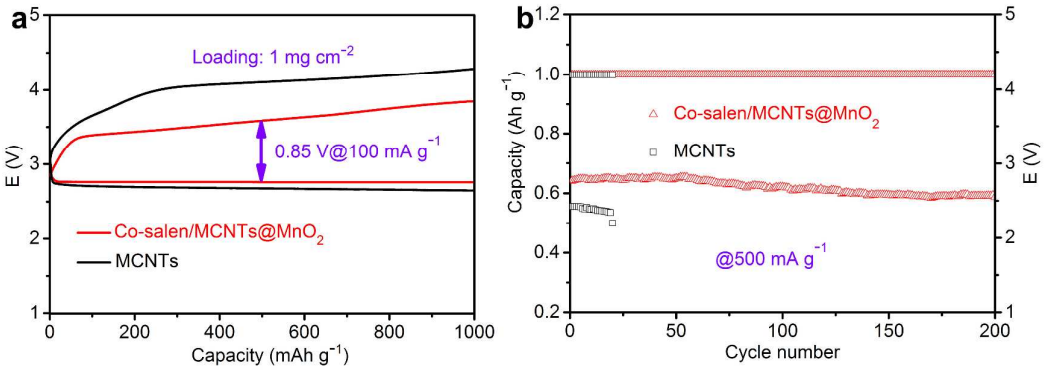


**Figure S13.** Battery performance in dry air with loading mass of 1 mg $cm^{-2}$. (a) Comparison of operating overpotentials at 100 mA $g^{-1}$ (0.10 mA $cm^{-2}$). (b) Cyclability comparison with controlled capacity of 1000 mAh $g^{-1}$ (1.0 mAh $cm^{-2}$) at 500 mA $g^{-1}$ (0.50 mA $cm^{-2}$).

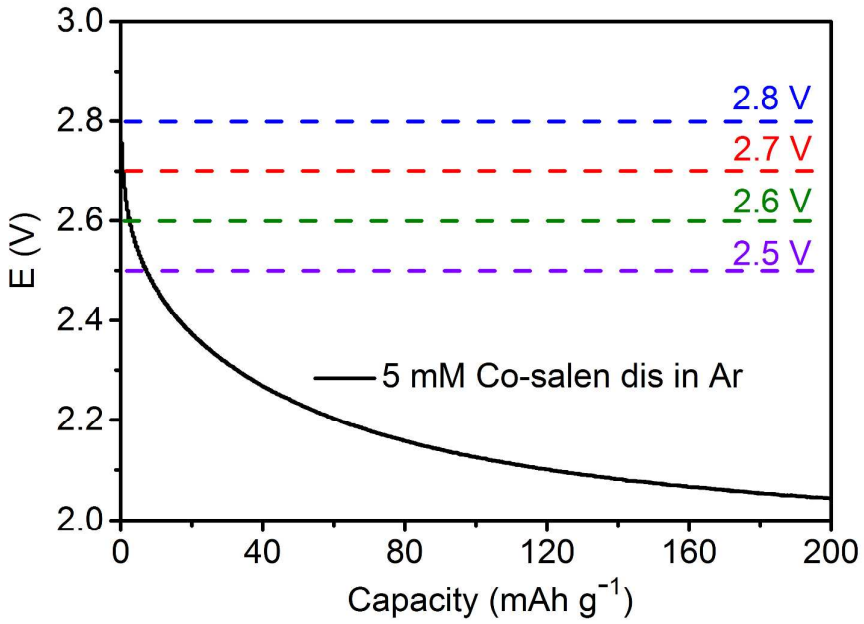


**Figure S14.** Discharge curve of LABs with Co-salen/MCNTs in Ar. Rate: 500 mA $g^{-1}$ (0.15 mA $cm^{-2}$).

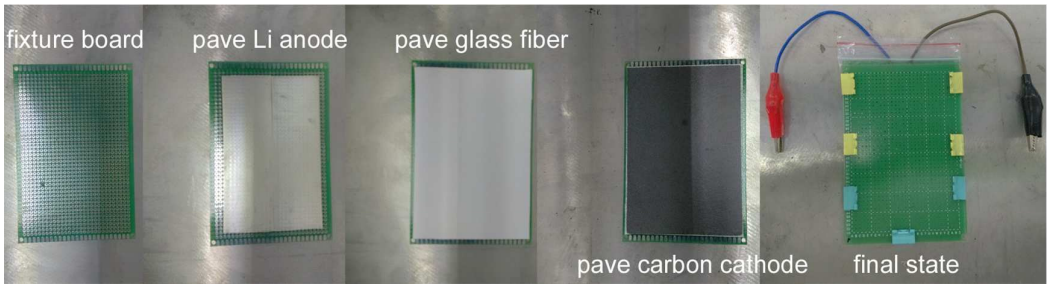


**Figure S15.** The assembly process of pouch-type LABs. Above glass fiber contains 5 mM Co-salen in 1 M LiTFSI/TEGDME.

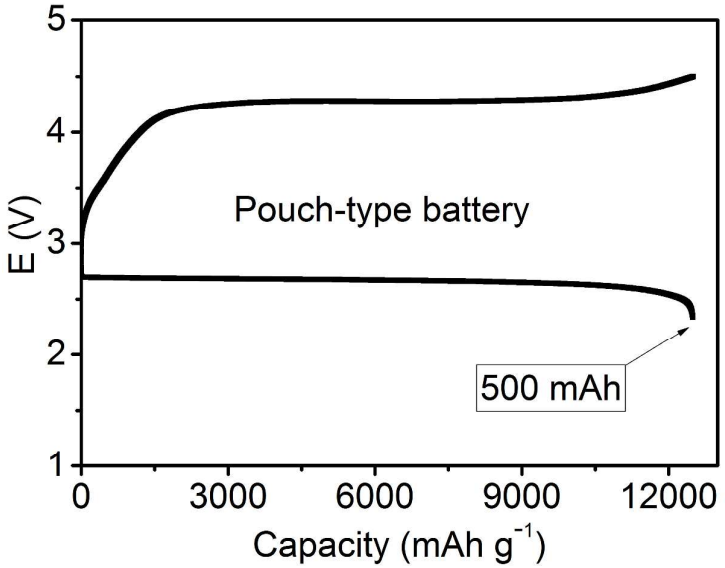


**Figure S16.** Discharge/charge profiles of pouch-type batteries.

Even though the charging overpotential of pouch-type LABs is higher than that of coin-type LABs, the charging process is also shown. The reversible discharge/charge capacity is 500 mAh, corresponding to 5.2 mAh $cm^{-2}$. In consideration of the total mass of the pouch-type battery is 4 g, the reversible capacity is 120 mAh $g^{-1}$. Optimizing the assembling technology is necessary to improve reversible capacity and reduce overpotentials.

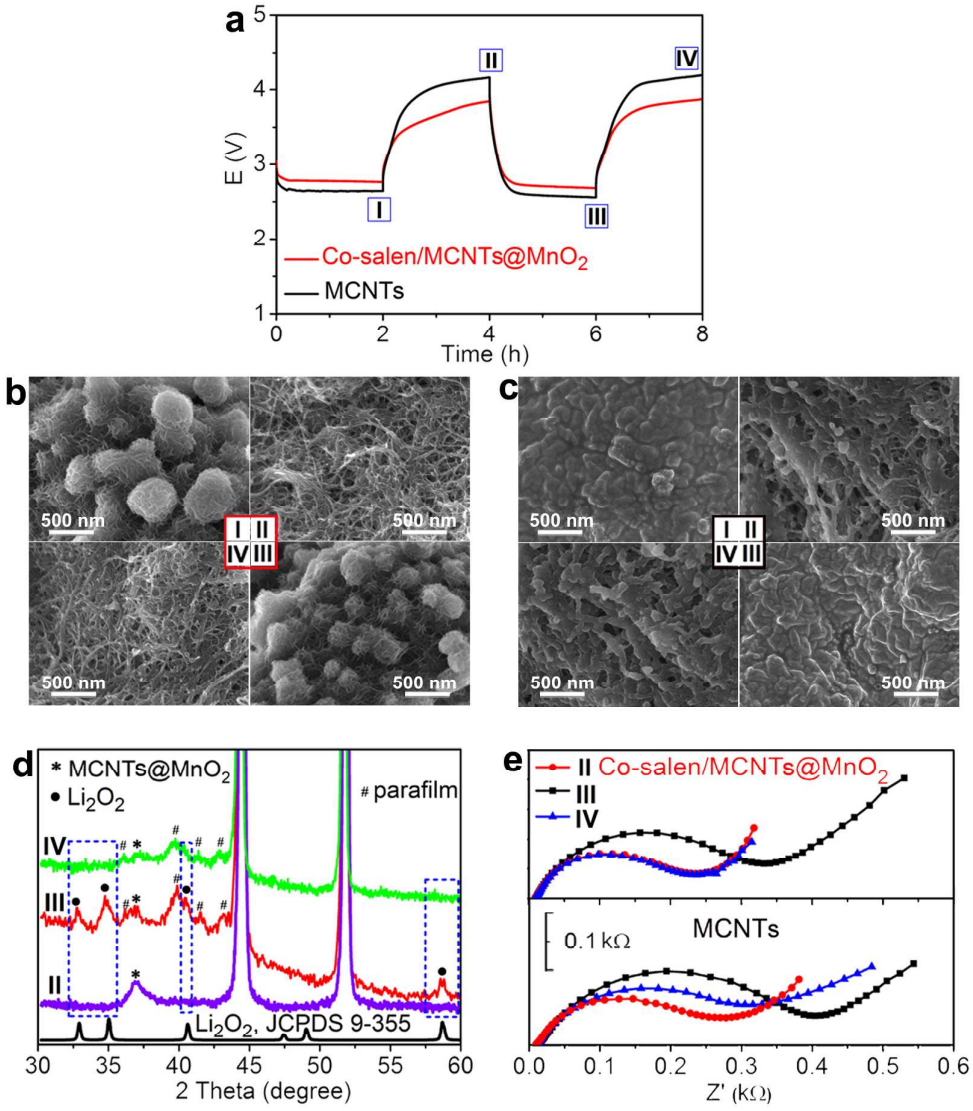


**Figure S17.** Process analysis of LABs with Co-salen/MCNTs@$MnO_2$ or only MCNTs. (a) Discharge and charge curves at 500 mA $g^{-1}$ with and without catalysts. (b,c) SEM images of cathode at different states with different catalytic conditions, (b) Co-salen/MCNTs@$MnO_2$, (c) MCNTs. (d) XRD patterns. The parafilm is used to keep air off. (e) Impedance spectra of LABs with MCNTs and Co-salen/MCNTs@$MnO_2$.

In order to verify the superior rechargeability of LABs with two-catalyst system of Co-salen/MCNTs@$MnO_2$, the cathode was dismantled from the batteries and analyzed at 4 different discharge/charge states and the LABs with only MCNTs act as the counterpart (Figure S17a). After discharge to 1000 mAh $g^{-1}$, the MCNTs@$MnO_2$ cathode is covered by echinus-like product with diameter of ~500 nm (state I). After recharging, the uniformly stacked product vanishes (state II). With LABs cycling, echinus-like product repeatedly appear and disappear (state III and state IV) (Figure S17b), suggesting the high catalytic efficiency of Co-salen/MCNTs@$MnO_2$ system towards ORR and OER. On the contrary, the discharge product

of MCNT cathode is aggregated and residuals are still can be observed on MCNT surface after charging or recharging (Figure S17c), indicating the difficulty on decomposing discharge products. The morphology difference of discharge products also confirms that two-catalyst system of Co-salen/MCNTs@$MnO_2$ accelerates $Li_2O_2$ formation in electrolyte.

The discharged/charged cathodes of the LABs with $Co^{II}$-salen in the electrolyte and operated in dry air were analyzed by X-ray diffraction (XRD) (Figure S17d). The reversible formation and decomposition of $Li_2O_2$ in the discharging and charging processes can be monitored by its characteristic diffraction peaks in comparison with the standard $Li_2O_2$. This is in accordance with the discharge/charge profiles in Figure S17a. In electrochemical impedance spectroscopic analysis (EIS) of LABs with Co-salen/MCNTs@$MnO_2$, the charge-transfer resistance ($R_{ct}$) is increased from 230 to 330 Ω after the first discharge. While, $R_{ct}$ is recovered to 232 Ω after charge. This indicates reversible generation and decomposition of $Li_2O_2$ at the cathode surface.[14] In comparison, the impedance of MCNT based LABs endured 245, 365, 320 Ω at pristine, discharged, and recharged states, respectively (Figure S17e). The unrecovered $R_{ct}$ agreed well with the recharged cathode containing residuals in Figure S17c (state IV) due to insufficient OER ability.

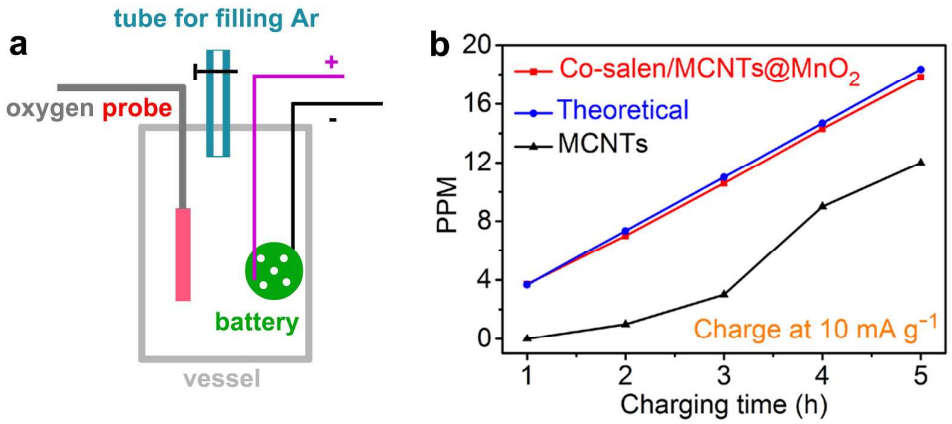


**Figure S18.** (a) Quantitative detection of $O_2$ during battery charging at 10 mA $g^{-1}$. (b) OER test of LABs with different catalytic conditions.

Quantitative detection of $O_2$ is carried out in a vessel with 500 mL of Ar. A discharged battery with or without 5 mM Co-salen and an $O_2$ probe (TAMASAKI, B-506, ± 0.01 ppm) are in the vessel. Quantitative detection of $O_2$ during battery charging is also carried out. The LABs with two-catalyst system of Co-salen/MCNTs@$MnO_2$ actually produce $O_2$, the amount of which is close to its theoretical value (3.56 ppm $min^{-1}$). This shows a much higher OER efficiency than that with only MCNTs.

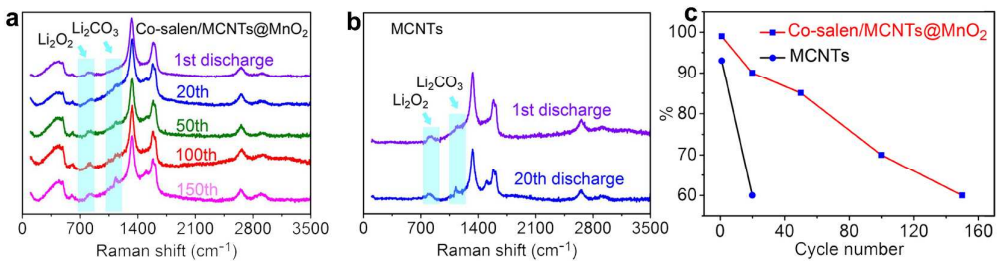


**Figure S19.** Chemical yields of LABs with different catalytic systems. (a,b) Raman spectra of cathodes in LABs with (a) Co-salen/MCNTs@$MnO_2$ and (b) MCNTs. (c) Mass percent of $Li_2O_2$ in discharge products of $Li_2O_2$ and $Li_2CO_3$.

The Raman (DXR 633 nm laser) indicates that the LABs with both MCNTs and two-catalyst system after the 1st discharge are dominated by $Li_2O_2$; while, after the 20th discharge, Raman offers solid evidence of serious side reactions on the MCNT cathode. In addition to $Li_2O_2$ (~790 $cm^{-1}$), the peaks at ~1100 $cm^{-1}$ are assigned to $Li_2CO_3$. On the contrary, significantly weaker Raman peak of $Li_2CO_3$ is observed on the cathode with two-catalyst system after the 20th discharge. This may stem from the trace of $CO_2$ in dry air and the partial decomposition of the TEGDME-based electrolyte. We here use integral areas of Raman peaks to roughly calculate chemical yields of $Li_2O_2$. After the 1st discharge, the chemical yields are 99% and 93% in LABs with Co-salen/MCNTs@$MnO_2$ and only MCNTs, respectively. In sharp contrast, the chemical yields of $Li_2O_2$ in Co-salen/MCNTs@$MnO_2$ system is 60% after the 150th discharge, which is close to that of MCNT based LABs after 20 cycles. The obvious difference in chemical yield shows an effective suppression of side reactions due to the two-catalyst system of Co-salen/MCNTs@$MnO_2$ in comparison with MCNTs. How to circumvent or restrain the formation of $Li_2CO_3$ during long cycles in dry air (or ambient air with 300 to 400 ppm of $CO_2$) is currently a material and technology challenge.

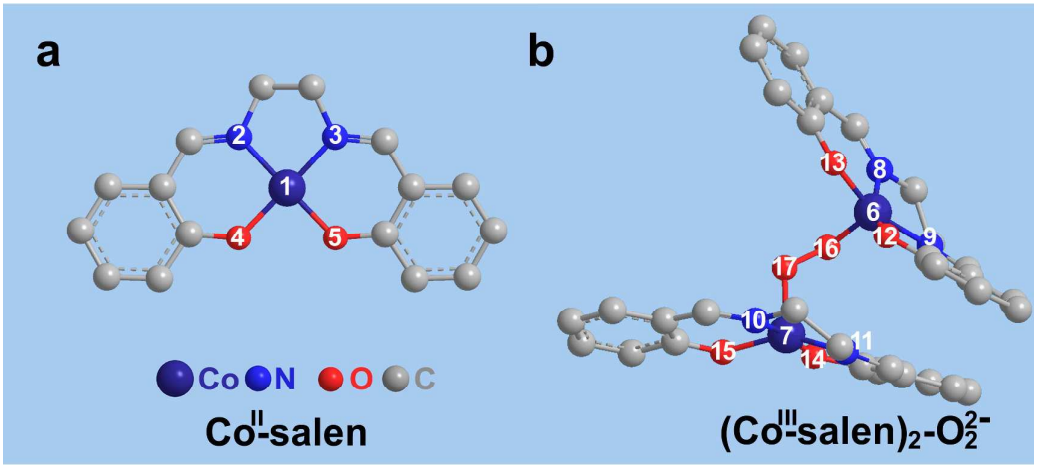


**Scheme S1.** DFT calculation on the molecular structure optimization of (a) $Co^{II}$-salen and (b) $(Co^{III}\text{-salen})_2\text{-}O_2^{2-}$.

**Table S1.** Bond lengths (Å) of $Co^{II}$-salen and $(Co^{III}\text{-salen})_2\text{-}O_2^{2-}$.

| | | | | | |
|---|---|---|---|---|---|
| Co(1)-N(2) | 1.86 | Co(6)-N(9) | 1.84 | Co(7)-O(15) | 1.86 |
| Co(1)-N(3) | 1.86 | Co(6)-O(12) | 1.88 | Co(7)-O(17) | 1.77 |
| Co(1)-O(4) | 1.84 | Co(6)-O(13) | 1.84 | Co(7)-N(10) | 1.84 |
| Co(1)-O(5) | 1.84 | Co(6)-O(16) | 1.79 | Co(7)-N(11) | 1.85 |
| Co(6)-N(8) | 1.86 | Co(7)-O(14) | 1.84 | O(16)-O(17) | 1.48 |

**Table S2.** Bond angles (º) of $Co^{II}$-salen and $(Co^{III}\text{-salen})_2\text{-}O_2^{2-}$.

| | | | | | |
|---|---|---|---|---|---|
| N(2)-Co(1)-N(3) | 86.33 | N(9)-Co(6)-O(12) | 91.84 | N(10)-Co(7)-O(14) | 93.70 |
| N(3)-Co(1)-O(5) | 93.63 | N(8)-Co(6)-O(13) | 91.83 | O(14)-Co(7)-O(15) | 84.69 |
| N(2)-Co(1)-O(4) | 93.63 | O(12)-Co(6)-O(13) | 83.33 | Co(6)-O(16)-O(17) | 111.76 |
| O(4)-Co(1)-O(5) | 87.76 | N(10)-Co(7)-N(11) | 86.93 | Co(7)-O(17)-O(16) | 115.38 |
| N(8)-Co(6)-N(9) | 84.94 | N(11)-Co(7)-O(15) | 91.56 | | |

The DFT calculations were implemented in Gaussian 09 Software.[15] All the structures were optimized at the B3LYP[16,17] level with the 6-31G (d) basis set, following by the frequency analysis to assure the real local minima. DFT calculations were performed to investigate the interaction between $Co^{II}$-salen and $O_2$. According to previous research,[18] the $Co^{II}$-salen tends to form 2:1 adducts with $O_2$, which is indicated by the electrons transferred number of ORR. The optimized geometry for the 2:1 complex is shown in Scheme 1b. The O-O bond length ($d_{o\text{-}o}$) of coordinated oxygen molecule is 1.48 Å, which is much longer than that of $O_2$ (1.21 Å), indicating the activation of $O_2$. Furthermore, the coordinated O-O bond length is close to that of $O_2^{2-}$(1.55 Å) in $Li_2O_2$ and $Na_2O_2$, confirming the formation of [$Co^{III}$---$O_2^{2-}$---$Co^{III}$], which results in the excellent oxygen uptake capability of $Co^{II}$-salen. Thus, the activated $O_2$ can facilitate the following electrochemical reaction.

## References


(1) Zhang, N.; Zhao, Q.; Han, X. P.; Yang, J. G.; Chen, J. *Nanoscale* **2014**, *6*, 2827−2832.

(2) Oh, S. H.; Black, R.; Pomerantseva, E.; Lee, J. H.; Nazar, L. F. *Nat. Chem.* **2012**, *4*, 1004–1010.

(3) Cheng, F. Y.; Chen, J. *Nat. Chem.* **2012**, *4*, 962–963.

(4) Hu, X. F.; Han, X. P.; Hu, Y. X.; Cheng, F. Y.; Chen, J. *Nanoscale* **2014**, *6*, 3522–3525.

(5) Toupin, M.; Brousse, T.; Bélanger, D. *Chem. Mater.* **2004**, *16*, 3184–3190.

(6) Cheng, F. Y.; Zhang, T. R.; Zhang, Y.; Du, J.; Han, X. P.; Chen, J. *Angew. Chem. Int. Ed.* **2013**, *52*, 1–5.

(7) Zhang, L.-S.; Liang, X.-Q.; Song, W.-G.; Wu, Z.-Y. *Phys. Chem. Chem. Phys.* **2010**, *12*, 12055−12059.

(8) Yoon, W. S.; Balasubramanian, M.; Yang, X. Q.; Fu, Z. G.; Fischer, D. A.; McBreen, J. *J. Electrochem. Soc.* **2004**, *151*, A246−A251.

(9) Zhou, J. G.; Hong, D.; Wang, J.; Hu, Y. F.; Xie, X. H.; Fang, H. T. *Phys. Chem. Chem. Phys*. **2014**, *16*, 13838−13842.

(10) Zhou, J. G.; Fang, H. T.; Hu, Y. F.; Sham, T. K.; Wu, C. X.; Liu, M.; Li, F. J. Phys. Chem. C **2009**, *113*, 10747−10750.

(11) Montoro, L. A.; Abbate, M.; Rosolen, J. M. *Electrochem. Solid-State Lett.* **2000**, *3*, 410−412.

(12) Uchimoto, Y.; Sawada, H.; Yao, T. *J. Power Sources* **2001**, *97*, 326−327.

(13) Yoon, W. S.; Chung, K. Y.; Nam, K. W.; Kim, K. B. *J. Power Sources* **2006**, *163*, 207−210.

(14) Gerbig, O.; Merkle, R.; Maier, J. *Adv. Mater.* **2013**, *25*, 3129–3133.

(15) Frisch, M. J.; Trucks, G. W.; Schlegel, H. B.; Scuseria, G. E.; Robb, M. A.; Cheeseman, J. R.; Scalmani, G.; Barone, V.; Mennucci, B.; Petersson, G. A.; Nakatsuji, H.; Caricato, M.; Li, X.; Hratchian, H. P.; Izmaylov, A. F.; Bloino, J.; Zheng, G.; Sonnenberg, J. L.; Hada, M.; Ehara, M.; Toyota, K.; Fukuda, R.; Hasegawa, J.; Ishida, M.; Nakajima, T.; Honda, Y.; Kitao, O.; Nakai, H.; Vreven, T.; Montgomery, J. A.; Jr., Peralta, J. E.; Ogliaro, F.; Bearpark, M.; Heyd, J. J.; Brothers, E.; Kudin, K. N.; Staroverov, V. N.; Kobayashi, R.; Normand, J.; Raghavachari, K.; Rendell, A.; Burant, J. C.; Iyengar, S. S.; Tomasi, J.; Cossi, M.; Rega, N.; Millam, J. M.; Klene, M.; Knox, J. E.; Cross, J. B.; Bakken, V.; Adamo, C.; Jaramillo, J.; Gomperts, R.; Stratmann, R. E.; Yazyev, O.; Austin, A. J.; Cammi, R.; Pomelli, C.; Ochterski, J. W.; Martin, R. L.; Morokuma, K.; Zakrzewski, V. G.; Voth, G. A.; Salvador, P.; Dannenberg, J. J.; Dapprich, S.; Daniels, A. D.; Farkas, O.; Foresman, J. B.; Ortiz, J. V.; Cioslowski, J.; Fox, D. J. Gaussian, Inc., Wallingford CT, **2009**.

(16) Becke, A. D. *J. Chem. Phys.* **1988**, *88*, 1053–1062.

(17) Lee, C.; Yang, W.; Parr, R. G. *Phys. Rev. B* **1988**, *37*, 785–789.

(18) Jones, R. D.; David, A. S.; Fred, B. *Chem. Rev.* **1979**, *79*, 139–179.